Localized magnetization reversal processes in cobalt nanorods with different aspect ratios

Marc Pousthomis, Evangelia Anagnostopoulou, Ioannis Panagiotopoulos, Rym Boubekri, Weiqing Fang, Frédéric Ott, Kahina Aït Atmane, Jean-Yves Piquemal, Lise-Marie Lacroix, G. Viau

Localized magnetization reversal processes in cobalt nanorods with different aspect ratios

M. Pousthomis, E. Anagnostopoulou, I. Panagiotopoulos, R. Boubekri, W. Fang, F. Ott*, K. Aït Atmane, J.-Y. Piquemal, L.-M. Lacroix, G. Viau*

Université de Toulouse, CEA/CNRS, Université Paris Diderot, France ; University of Ioannina, Greece

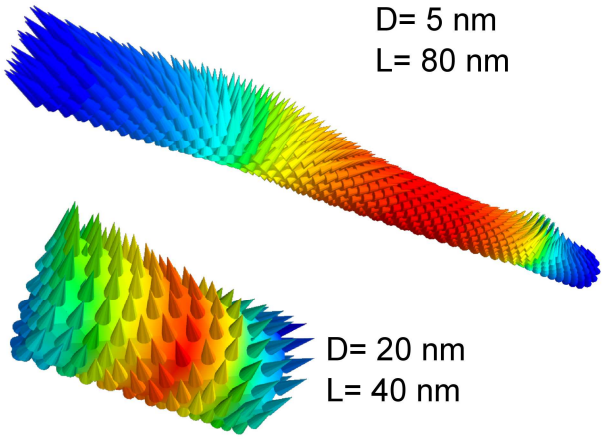

The diameter dependence of the coercivity of cobalt nanowires is quantitatively described by micromagnetic modelling, which reveals that the magnetization reversal is driven by nucleation at the edges or at stacking faults.

Nano Res
DOI (automatically inserted by the publisher)
Research Article

Localized Magnetization Reversal Processes in Cobalt Nanorods with Different Aspect Ratios

Marc Pousthomis[1], Evangelia Anagnostopoulou[1], Ioannis Panagiotopoulos[2,3], Rym Boubekri[1], Weiqing Fang[2], Frédéric Ott[2] (✉), Kahina Aït Atmane[4], Jean-Yves Piquemal[4], Lise-Marie Lacroix[1] and Guillaume Viau[1](✉)

[1] Université de Toulouse, INSA CNRS UPS, UMR 5215 LPCNO, 135 av de Rangueil, 31077 Toulouse Cedex 4, France
[2] Laboratoire Léon Brillouin, CEA/CNRS UMR12, IRAMIS, CEA-Saclay, 91191 Gif sur Yvette, France
[3] Department of Materials Science and Engineering, University of Ioannina, Ioannina 45110, Greece
[4] Université Paris Diderot, Sorbonne Paris Cité, ITODYS, CNRS UMR 7086, 15 rue J.-A. de Baïf, 75205 Paris Cedex 13, France

Received: day month year / Revised: day month year / Accepted: day month year (automatically inserted by the publisher)

ABSTRACT

We present results on the synthesis of cobalt nanorods by the polyol process and on the mechanism of magnetization reversal. We show that the nucleation step is very dependent on the nature of the ruthenium chloride used as nucleating agent. This allows varying independently the cobalt nanorods diameter and their aspect ratio. Co nanorods with respectively aspect ratio, mean diameter and mean length in the ranges AR_m = 3 - 16, D_m = 7 – 25 nm, and L_m = 30 – 300 nm, were produced by this method. X-ray diffraction and electron microscopy showed that a strong discrepancy between the structural coherence and the morphological aspect ratio can exist due to stacking faults. The coercivity of assemblies of different nanorods was systematically measured. The highest values were obtained for the smallest diameter and the largest structural coherence length. Micromagnetic simulations were performed to account for the dependence of the coercive field on the diameter. An important observation is that simple coherent magnetization rotation models do not apply for these magnetic nano-objects. Even for very small diameters (D_m = 5-10 nm), well below the theoretical coherent diameter D_{coh}(Co) = 24 nm, inhomogeneous reversal modes dominated by nucleation at the rod edges or at structural defects such as stacking faults are observed. The conclusion is that, in order to produce high coercivity materials based on nanowires, moderate aspect ratios of 5-10 are sufficient providing a structural coherence similar to the morphological aspect ratio. Thus, the first priority should be to avoid the presence of stacking faults within the Co nanowires.

KEYWORDS

nanorod, nanowire, permanent magnets, micromagnetic calculations, shape anisotropy

1. Introduction

Elongated inorganic nanoparticles exhibit properties that strongly differ from those of isotropic nanoparticles and are investigated in different fields such as optics, electronics, magnetism or catalysis [1]. The shape anisotropy of magnetic nanorods (NRs) and nanowires (NWs) makes these objects

interesting for applications in magnetic recording [2], biological sensors [3] or permanent magnets [4, 5]. In the field of permanent magnets, there is a great interest for new hard magnetic materials alternative to rare earth based magnets [6]. Bottom-up techniques for the fabrication of permanent magnets are emerging approaches thanks to the development of new nanoparticle syntheses [7, 8]. Among the different kind of nanoparticles, assemblies of oriented cobalt nanorods and nanowires are interesting candidates because their growth along the hexagonal c axis enables to benefit from magnetocrystalline and shape anisotropy. Thus their magnetization curve can exhibit both high squareness, high magnetization and high coercivity [9–11].

Several methods were reported in the literature for the fabrication of cobalt NRs and NWs, whose structure strongly depends on the preparation route. The first method is the electrochemical growth of cobalt in the uniaxial pores of an alumina matrix. This method gives parallel arrays of Co NWs with a mean diameter in the range 20-200 nm and very high length (> 1 μm). The NWs are generally polycrystalline [12, 13]. Recently, hcp Co NWs with different textures, [101], [002] and [110], were obtained by tuning the electroplating conditions [14]. A second method consists in pulsed-laser co-deposition of Co and CeO_2 epitaxial films on $SrTiO_3$ (001). Very thin Co NWs (mean diameter of about 3 nm) embedded in a CeO_2 matrix are formed spontaneously during the co-deposition [15]. The structural studies show polycrystalline NWs with a mixture of fcc and hcp phases. Finally, two chemical methods were developed for the growth of Co and CoNi NRs and NWs: the polyol process that consists in the reduction of a cobalt carboxylate in a liquid diol [9] and the organometallic approach that consists in the reduction of a coordination complex with hydrogen in an organic solvent [16,17]. These chemically grown nanowires crystallize with the hcp structure and the long axis of the wires is parallel to the hcp c axis. The mean diameter is comprised between 5 and 40 nm depending on the experimental conditions. For the polyol process the final shape is very dependent on the long chain carboxylate concentration. This effect is well described by theoretical calculations showing that the carboxylate ligand adsorption on the different facets of the hcp Co governs the anisotropic growth [18]. To the best of our knowledge the higher coercivity values at room temperature are obtained with Co NRs prepared by chemical processes [5]. Indeed their structure is such that the shape and magneto-crystalline anisotropy easy axes are parallel which increases the overall anisotropy [19].

On a theoretical point of view, the understanding of the magnetization reversal in elongated nanoparticles (nanowires and nanorods) is an interesting question that historically motivated analytical models [20] and was recently renewed thanks to the comparison of experimental measurements with numerical modelling on isolated rods or assemblies [14, 21–24]. In the simple Stoner Wohlfarth model, the expected shape anisotropy of a long Co nanowire is $\mu_0 H_{Shape} = \mu_0 M_{Co}/2 = 0.85$T. For a single crystalline hexagonal Co wire with its c-axis along the wire, there is an extra magneto-crystalline anisotropy $\mu_0 H_{MC} = 2K_{MC}/M_S = 0.74$T, assuming the bulk value for K_{MC}(Co). In such an ideal system, coercivity up to 1.59T would be expected. Experimental results are always far from these values, the highest observed coercivity being 1.03 T [5]. Our aim in this communication is to provide a thorough study of the parameters defining the coercivity of assemblies of Co nanowires and why the experimental values differ from theoretical expectations.

In this paper, we also present new results on the synthesis of Co nanorods by the polyol process. We show that it is possible to vary independently the mean diameter and the mean aspect ratio over a wide range. The structural properties of the rods are studied by X-ray diffraction. In order to figure out which objects (length, diameter and microstructure) have the best properties, the coercive field of wires assemblies randomly oriented and aligned have been systematically measured. Micromagnetic simulations have been performed to account for the dependence of the coercive field on the aspect ratio, diameter and structural properties of the nanowires.

2. Experimental

Cobalt acetate tetra hydrate was purchased from Alfa Aesar, sodium hydroxide and lauric acid from Acros, hydrated and anhydrous ruthenium chloride from Sigma-Aldrich. Cobalt nanorods (NRs) were synthesized by the polyol process according to a procedure previously published [9]. This synthesis included three steps: the synthesis of sodium laurate, the synthesis of cobalt laurate and finally the reduction of cobalt laurate in a basic solution of 1,2 butanediol.

2.1 Cobalt laurate synthesis

First, sodium laurate was synthesized by mixing stoichiometric amount of lauric acid and sodium hydroxide in de-ionized water at 85 °C. A white powder precipitated and was recovered by suction filtration. The solid was thoroughly washed with de-ionized water and dried overnight at 50 °C. The synthesis of cobalt laurate precursor was performed by dissolving separately cobalt acetate tetrahydrate and sodium laurate in de-ionized water and then mixing them with a mechanical stirrer until a pink homogeneous powder in suspension was obtained. By filtering the precursor and washing with de-ionized water, the slight excess of cobalt acetate that did not react was removed and finally, the pink fine powder was dried at 50 °C in order to remove the water excess. Two cobalt laurates could be isolated by this method: a dihydrated cobalt laurate, $Co(C_{11}H_{23}CO_2)_2,(H_2O)_2$ already described by Rabu et al. [25] and an anhydrous cobalt laurate $Co(C_{11}H_{23}CO_2)_2$ obtained with longer drying times. Both compounds present a layered structure with an interlayer spacing measured by X-ray diffraction of 36.8 Å and 34 Å for the dihydrated and the anhydrous compound, respectively. Thermogravimetric analyses (TGA) of the two compounds were performed in air from room temperature to 600°C, temperature at which the laurates are totally transformed into Co_3O_4. The TGA of the di-hydrated cobalt laurate showed a first weight loss of about 6% at 100°C, in good agreement with the presence of two water molecules in the formula (calculated value 7.3%), followed by a second weight loss of 76-77 % in the temperature range 200-450 °C. The total weight loss was between 82 and 83% (calculated value 83.7%). TGA analysis of the anhydrous cobalt laurate showed a single weight loss between 79.5 and 82.4 % (calculated value 82.2%) in the temperature range 200-450°C. The chemical analysis of the anhydrous cobalt laurate gave a mass content in carbon and hydrogen of 61.2 and 10.6%, respectively. These values are very close to the calculated values of 63 and 10% for the expected formula $Co(C_{11}H_{23}CO_2)_2$.

2.2 Cobalt nanorods synthesis

Anhydrous cobalt laurate was dispersed in a sodium hydroxide solution of 1,2-butanediol. The concentration of cobalt was 8 x 10-2 M in all experiments. The NaOH concentration was 7.5 x 10-2 M. Ruthenium chloride was added in the medium to control the nucleation step. The ratio [Ru]/[Co] = 2.5% was fixed in all the experiments. Three different ruthenium chlorides were used: two types where hydrated, $RuCl_3 \cdot xH2O$, with 99.8% of trace metals (ref. Sigma Aldrich 463779) and 38-42% Ru basis (ref. Sigma Aldrich 84050) and one was anhydrous, $RuCl_3$ (ref. Sigma Aldrich 208523). Classic heating mantle or microwaves were used as heating systems. The suspension of cobalt laurate in the basic solution of butanediol containing the ruthenium chloride was heated to 175 °C for 30 min. The solution turned to black indicating the cobalt reduction. The temperature slope was fixed at 8 $°C.min^{-1}$ in the classical setup and was varied in the range 8-150 $°C.min^{-1}$ with the microwave equipment. The cobalt particles were recovered by centrifugation and washed twice with absolute ethanol and once with chloroform before characterizations.

2.3 Ruthenium chloride characterizations

Thermogravimetric analyses of the three ruthenium chlorides were performed in air from room temperature to 800°C. The TGA of anhydrous RuCl3 (ref. Sigma Aldrich 208523) showed a first weight loss of about 4% at 100°C corresponding to physisorbed water, and a second weight loss of about 30% at 360°C corresponding to the departure of the chlorine atom and the formation of ruthenium oxide. The TGA of the two hydrated ruthenium chlorides exhibit a continuous weight loss between room temperature and 300°C followed by a steep

weight loss at 360°C. The first weight loss is about 7% and 12% for the RuCl3 Sigma Aldrich 84050 and 463779, respectively. The very broad temperature range in which the first weight loss occurs is in agreement with the presence of ruthenium hydroxychloride complexes in the two hydrated ruthenium chlorides. The amount of these species is more important in the compound ref. 463779 according to the larger weight loss. The difference between the TGA of the three RuCl3 in the range 100-300°C is thus interpreted as an absence of ruthenium hydroxychloride in the anhydrous compound (ref. 208523) and as the presence in different amount in the two hydrated compounds.

2.4 Cobalt nanorods characterizations

The cobalt nanorods were characterized by transmission electron microscopy (TEM) using a Jeol JEM 1400. Mean diameter (D_m), mean length (L_m) and mean aspect ratio ($AR_m = L_m/D_m$) were measured from the image analysis on c.a. 200 rods. X-ray diffraction (XRD) patterns were recorded on a PANalytical Empyrean diffractometer using the Co Kα radiation. The line broadening (full width at half-height) was measured using the Highscore software and was corrected for the instrumental broadening measured on a Si standard sample. The crystallite size was inferred from the corrected line broadening using the Scherrer formula. The magnetic properties of the cobalt nanorods were measured at room temperature using a Vibrating Sample Magnetometer (VSM). The as-synthesized NRs were washed twice in ethanol and dispersed in tetracosane. The rod volume fraction was in the range 0.5-1% (weight fraction 5-6 %). Alignment was performed in an external magnetic field of 5 T above the melting point of tetracosane (330 K) as reported in [10]. The oriented wires were then frozen by cooling the tetracosane at 300K.

3. Results and Discussion

3.1 Morphology

It is now well established that the morphology of the cobalt particles prepared by the polyol process depends on several parameters: the nature of the cobalt precursor, the α-diol, the heating rate and the basicity of the solution [9,18,26]. In this study we report on the possibility of varying the aspect ratio of Co NRs by playing upon the nature of the ruthenium chloride precursor that acts as nucleating agent.

A typical experiment consists in the reduction of anhydrous cobalt laurate in a $7.5x10^{-2}$ M NaOH in 1,2 butanediol at 175°C with a heating rate of 8°C.min-1. With the $RuCl_3 \cdot xH2O$ precursor (ref. Sigma Aldrich 463779), cobalt nanorods with a mean diameter in the range D_m = 16-25 nm and a mean length in the range L_m = 200-350 nm were obtained. The mean aspect ratio AR_m was generally higher than 10 (Fig. 1a). Cobalt nanorods with smaller mean diameters, in the range 15-20 nm and smaller mean length, in the range 100-200 nm, were obtained when the $RuCl_3 \cdot xH_2O$ (ref. Sigma Aldrich 84050) was used as a nucleating agent. The mean aspect ratio ARm was in the range 7-12 (Fig. 1b). The smallest NRs with a mean diameter inferior to 10 nm and a mean aspect ratio in the range 3-8 were obtained with the anhydrous $RuCl_3$. Nevertheless, with this nucleating agent, polydisperse particles were obtained when the heating rate was lower than 20 °C.min^{-1}. By increasing the heating rate to values in the range 50-150 °C.min^{-1}, using a microwave equipment, monodisperse nanorods with D_m = 7 nm and a mean aspect ratio AR_m in the range 4-5 were obtained (Fig. 1c). In the general scheme describing the formation of cobalt nanorods by the polyol process, the role of the small amount of ruthenium is to generate in situ small metal seeds for the cobalt growth [9]. The final shape of the particles is expected to depend on the seed concentration in the medium. A first approach consists in varying the relative concentration of the ruthenium precursor, as previously reported for anisotropic $Co_{80}Ni_{20}$ particles [27]. Here we show that it is possible to modify the morphology of Co NRs by varying solely the nature of the ruthenium chloride introduced in the medium, the relative concentration of Ru being kept constant ([Ru]/[Co] = 2,5%). Indeed, depending on the nature of the ruthenium chloride, the number of ruthenium seeds produced in the medium can strongly vary. The TGA characterization

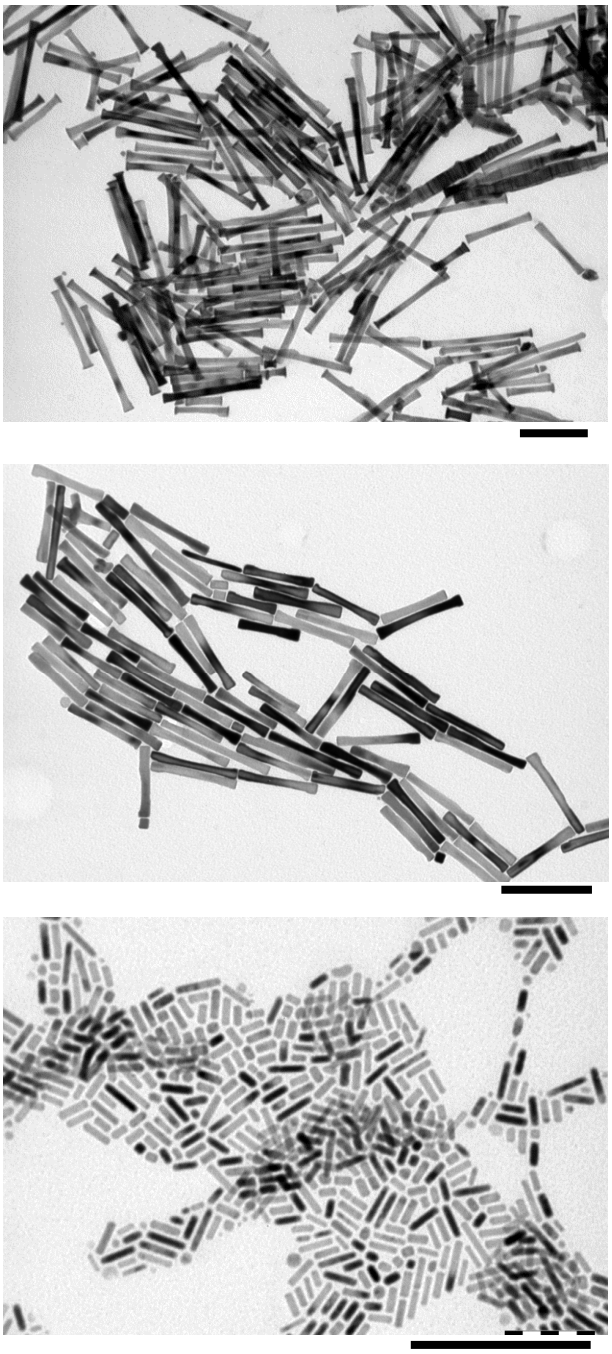

Figure 1 Representative TEM images of cobalt nanorods synthesized with (a) classical heating mantle, 8°C.min^{-1}, 2.5% of hydrated $RuCl_3$ ref. Sigma Aldrich 463779; (b) classical heating mantle, 8°C.min^{-1}, 2.5% of hydrated $RuCl_3$ ref. Sigma Aldrich 84050 ; (c) microwave heating 50°C.min^{-1}, 2.5% of anhydrous $RuCl_3$ ref. Sigma Aldrich 208523 (Scale bar denotes 200 nm). Mean diameter, D_m, and mean length, L_m: (a) D_m = 18 nm, L_m = 280 nm; (b) D_m = 16 nm, L_m = 160 nm; (c) D_m = 7.5 nm, L_m = 28 nm.

(see experimental section) showed strong variations of the hydroxychloride content in the different ruthenium precursor in the following order ref. 208523 < ref. 84050 < ref. 463779. This chemical composition variation may be at the origin of a difference of reactivity and therefore of the reduction rate. According to the final volume of the nanorods, the nucleation rate of the $RuCl_3$ precursors follows the order: ref. 208523 > ref. 84050 > ref. 463779. The anhydrous ruthenium chloride produces much more seeds than the hydrated ruthenium chlorides, resulting in the formation of the smallest nanorods. The shorter nanorods obtained with the hydrated ruthenium chloride ref. 84050 compared to the long rods obtained with the hydrated ruthenium chloride ref. 463779 can also be explained by a higher nucleation rate due to a lower hydroxychloride content. Thus, the nucleation rate of the Ru precursor, critical to tune the nanorods diameter, seems to be inversely proportional to the hydroxychloride content. The lower the hydroxychloride content is, the smallest the rod diameters are. Another consequence of the higher nucleation rate and higher growth rate on the nanorods is the shape of the tip. The rods prepared with the anhydrous ruthenium chloride have a round tip whereas the rods prepared with the hydrated ruthenium chloride have a larger tip.

3.2 Structure

The XRD patterns show that the cobalt NRs crystallize with the hcp structure. The broadening of the XRD line is strongly dependent on the (hkil) indexes, indicating a strong anisotropy of the crystallite growth. The (0002) line is always much narrower than the $(10\bar{1}0)$ line (Fig. 2a) in good agreement with a longer crystallographic coherence along the c axis, thus revealing that the rod growth axis is parallel to the crystallographic c axis, as previously reported [28]. The crystallite size $L_{(10\bar{1}0)}$ measured for the $(10\bar{1}0)$ planes using the Scherrer equation was always found very close to the particle mean diameter measured by TEM. It is well known that the density of faults in the (ABAB) hcp stacking can strongly vary depending on the growth conditions [26]. When the staking fault density is important a significant additional broadening of the

$(10\bar{1}1)$ line compared to the $(10\bar{1}0)$ line is observed [26]. This is not the case for the samples synthesized here. No significant broadening of the $(10\bar{1}1)$ line compared to the $(10\bar{1}0)$ line was observed showing a low density of stacking faults. Nevertheless, the crystallographic coherence along the c axis $L_{(0002)}$, deduced from XRD, was always found smaller than the rod mean length L_m, deduced from TEM. In the figure 2b, $L_{(0002)}$ value is plotted as a function of L_m for different samples. For the shortest rods (< 150 nm) $L_{(0002)}$ is about one half of the L_m value. On the other hand for the longest rods (> 250 nm) scattered $L_{(0002)}$ values are observed. Thus, an increase of the rod mean length does not automatically lead to an increase of the crystallographic coherence length along the c axis, but can induce additional defects. These defects may have a strong influence on the magnetic properties. Therefore the magnetic properties, reported in the next section, have been analyzed not only as a function of the morphological aspect ratio (AR_m) but also as a function of the structural coherence aspect ratio defined as $L_{(0002)}/ L_{(10\bar{1}0)}$.

3.3 Magnetic properties

Both magneto-crystalline and shape anisotropies being along the nanowires long axis, the magnetization easy-axis lays parallel to the nanorods axis. It is thus possible to easily align the Co NRs by applying an external magnetic field. The coercivity of randomly oriented rods and aligned rods are reported in Figure 3a. Before alignment (red diamonds), the ratio of remanence to saturation magnetization M_r/M_S is 0.50, as expected for randomly oriented single-domain uniaxial particles [4]. After alignment (Fig. 3a) the magnetization curves measured parallel to the aligned wires have a square shape with M_r/M_S > 0.80. This increase of coercivity can be qualitatively explained according to the Stoner-Wohlfarth (SW) model [4].

We have systematically measured the coercivity (H_C) for Co nanorods with different mean aspect ratios and mean diameters. The volume fraction of the rods was the same in all samples. Thus, we assumed that the dipolar interactions were similar. The results are

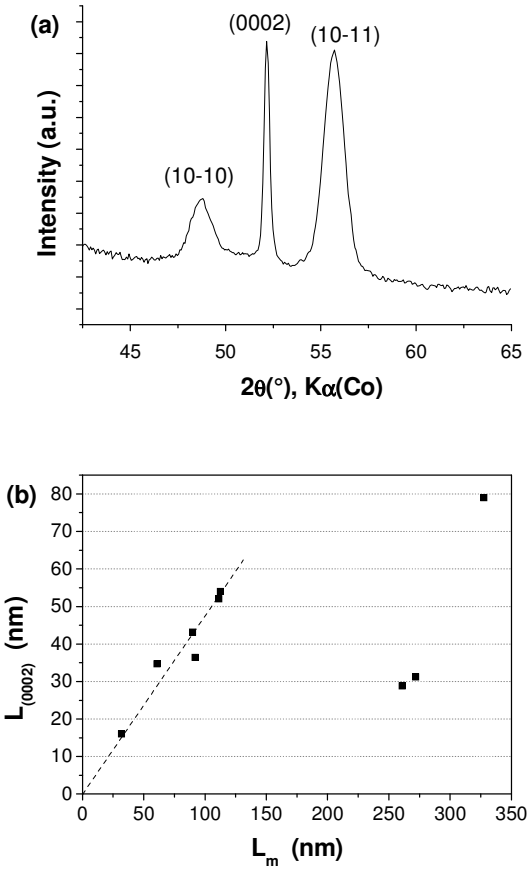

Figure 2 (a) X-ray diffraction pattern of Co nanorods (D_m = 9 nm, L_m = 62 nm measured by TEM). Mean crystallite sizes of $L_{(10\bar{1}0)}$ = 7 nm and $L_{(0002)}$ = 35 nm were inferred from the X-ray line broadening; (b) Variation of the crystallographic coherence along the c axis $L_{(0002)}$ for cobalt nanorods with different mean length.

summarized in Figure 3b. The coercivity of the randomly oriented rods is in the range $\mu_0 H_C$ = 0.2 – 0.6 T and those of aligned rods in the range $\mu_0 H_C$ = 0.3 - 0.72 T. For aspect ratios ARm in the range 2-10, the coercivity increases with the aspect ratio in agreement with an enhanced shape anisotropy [21]. However, for higher aspect ratios (above 12), no gain is observed, as expected within the standard SW model (see Figure 4, red curve), the measured coercivities are even reduced.

This decrease may results from structural imperfections. Indeed stacking faults are known to reduce the coercivity in nanosized magnetic entities by providing nucleation points due to a locally reduced magneto-crystalline anisotropy [29]. For the

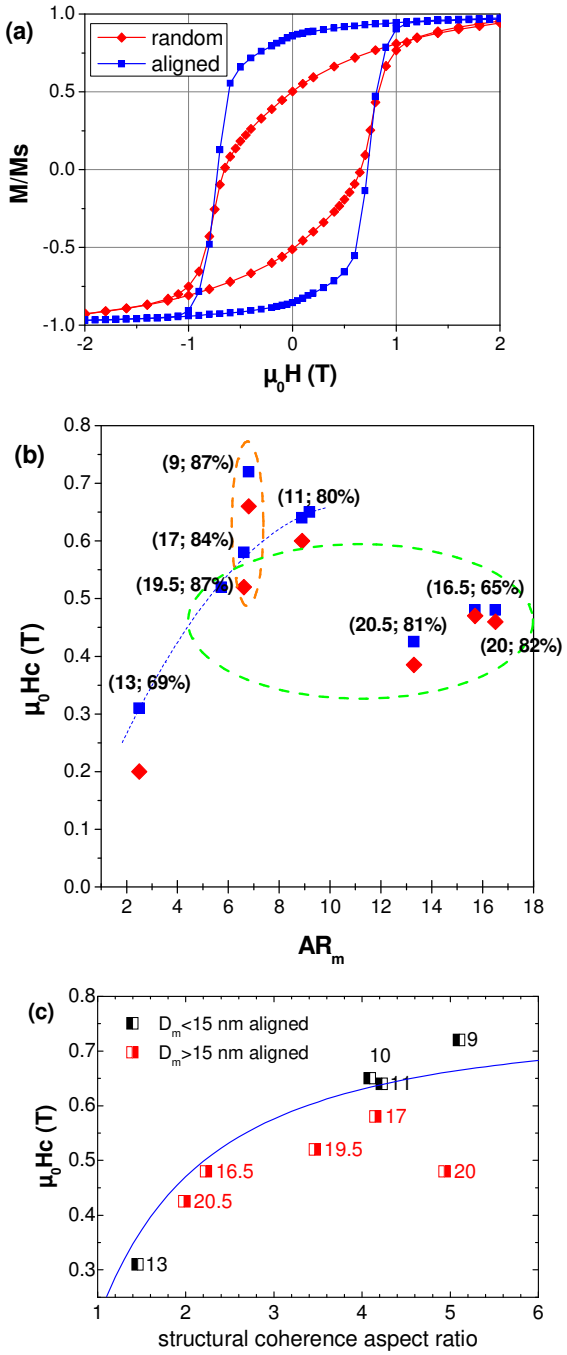

Figure 3 (a) Hysteresis loops of cobalt nanorods (D_m = 9 nm; L_m = 62 nm) measured on randomly oriented (red diamonds) and aligned wires (blue squares). The field was applied along the wires axis (easy axis) in the latter case ; (b) Coercivity of assemblies of Co nanorods vs. morphological aspect ratio AR_m for different samples: aligned (blue squares) or randomly oriented (red diamonds). (mean diameter Dm ; remanence Mr/Ms for the aligned rods) are given for each sample; (c) Coercivity of different nanorods assemblies aligned vs structural aspect ratio calculated as $L_{(0002)}/L_{(10\bar{1}0)}$. The larger diameter samples are indicated by red colour. Numbers D_m indicate diameter in nm. The blue line is a guide-to-the-eye.

samples with L_m > 250 nm on Fig 2b, corresponding to morphological aspect ratio AR_m > 12 on Fig.3b, the structural aspect ratio $L_{(0002)}/L_{(10\bar{1}0)}$ can be much lower (as low as 2 for some samples). Therefore, the longer rods may exhibit more defects than the shorter one, explaining the decrease of coercivity observed. To further underline the correlation between the magnetic properties and the structural properties, the coercivity is plotted in figure 3c as a function of the structural aspect ratio $L_{(0002)}/L_{(10\bar{1}0)}$. The coercivity of the thinnest rods (in black) steadily increases with the $L_{(0002)}/L_{(10\bar{1}0)}$ ratio. On the other hand, the bigger rods (D_m ~ 20 nm, in red) exhibit always lower coercivities than the thinner ones even for comparable structural aspect ratios and equivalent alignment, shown by the M_r/M_S ratio which ranges from 0.84 to 0.87. This suggests that even if the wires diameters are in theory below the limit of uniform magnetization reversal (D_{coh} = 25 nm, see next section), non uniform magnetization reversal processes are taking place. This is further supported
by the fact that for the large diameter wires, the wires alignment does not provide any significant increase in the coercive field suggesting that the magnetization reversal nucleation occurs irrespective of the wire orientation. This is contradictory with a coherent reversal process. To investigate the magnetization reversal mechanism we have thus performed micro-magnetic simulations.

3.4 Micromagnetic simulations

In single domain particles the reversal process is not necessarily uniform and cannot be simply described by the Stoner-Wohlfarth model. Depending on the diameter and length other collective reversal modes, such as curling or buckling, may occur, which ease the reversal process and reduce the coercive field. For larger particles the reversal may even take place via localized (not-collective) modes, namely nucleation and domain wall propagation. In spherical particles, it is traditionally considered that coherent or uniform rotation occurs when the particle radius is smaller than $R_{coh} = \sqrt{24}\, l_{ex}$ [30], where the exchange length $l_{ex} = \sqrt{A/\mu_0 M_S^2}$. In the

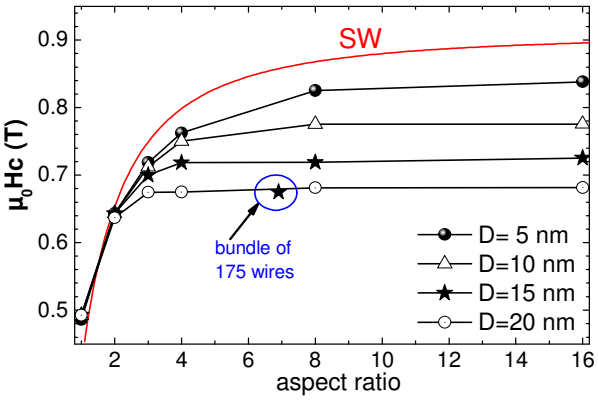

Figure 4 Coercivity values of Co cylinders with different diameters D as a function of their aspect ratio. The external field was applied at 22° with respect to the cylinder axis. The prediction of the Stoner-Wohlfarth (SW) model is plotted as a red continuous line.

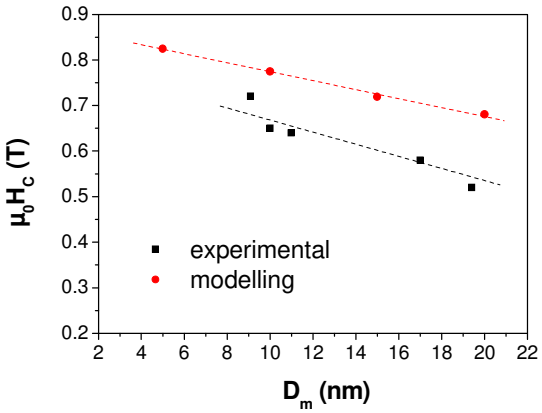

Figure 5 Coercivity vs mean diameter of nanorods: (red) calculated for an aspect ratio of 8 (the external field was at 22° with respect to the cylinder axis); (black) measured on aligned nanorods exhibiting an aspect ratio between 6 and 9 and a structural coherence aspect ratio between 3.5 and 5.

case of long cylinders, the limiting radius for coherent rotation is smaller and can be derived as $R_{coh} = 3.65\, l_{ex}$. In the case of cobalt, using an exchange constant A = 2.8x10^{-11} J.m^{-1}, l_{ex} = 3.4nm, the coherent radius is on the order of R_{coh} =12.3 nm. It is also possible to define a single domain radius above which the reversal proceeds by domain wall propagation $R_{SD} = 64\frac{l_{ex}^2}{\pi\delta}$ where $\delta = \sqrt{A/K}$ is the wall width parameter. For cobalt, R_{SD} can be estimated as 31 nm. Thus for our wires, the physical radius would be expected to be below the theoretical coherent radius R_{coh}. We are also in principle well below the single domain radius R_{SD}. Note however that these limits are only rough estimates assuming perfect geometries. The numerical values are also very dependent on the value of A. Thus in order to assess the details of the magnetization reversal processes in these wires and check what are the dominant reversal mechanisms, micromagnetic simulations have been performed with the nMag package [31]. The bulk Co parameters (M_S = 1.4 MA.m^{-1}, K_U = 520 kJ.m^{-3}, A = 28 pJ.m^{-1}) have been used.

A series of simulations on individual wires of cylindrical shape with different diameters and aspect ratios was performed to establish the H_C dependence on these geometrical factors. The external field was misaligned by an angle ψ = 22° with respect to the cylinder axis. This value corresponds to the standard deviation of a Gaussian distribution of the misalignment angle that yields M_r/M_S = 0.85. The results are shown in Figure 4 in comparison with the Stoner-Wohlfarth (SW) model prediction. The Figure 4 shows that for larger diameters (D ~ 20 nm), the H_C values are substantially smaller from those expected with the SW model and furthermore their dependence on the aspect ratio is suppressed. This indicates that the benefit of shape anisotropy is lost when the diameter increases. For a fixed aspect ratio (above 8) the coercivity drops almost linearly between D = 5 nm and 20 nm. A comparison of the H_C values calculated for the aspect ratio of 8 and the experimental H_C measured with samples of mean aspect ratio comprised between 6 and 9 is given in Figure 5. The calculated H_C values are comparable to those experimentally observed, taking into account that for dense assemblies of nanowires with some size and orientation distributions a further reduction close to 10% occurs. This is a result of the dipolar inter-particle interactions which in a random assembly tend to favour nucleation events. As an example the coercivity of a bundle of 175 wires with L = (100 ± 20) nm and D = (15 ± 2) nm is also included on Figure 4 (point in the blue ellipse).

In order to elucidate the difference between the underlying reversal mechanisms in large and small diameter wires, the evolution of the magnetic state close to H_C was monitored as a function of time. The

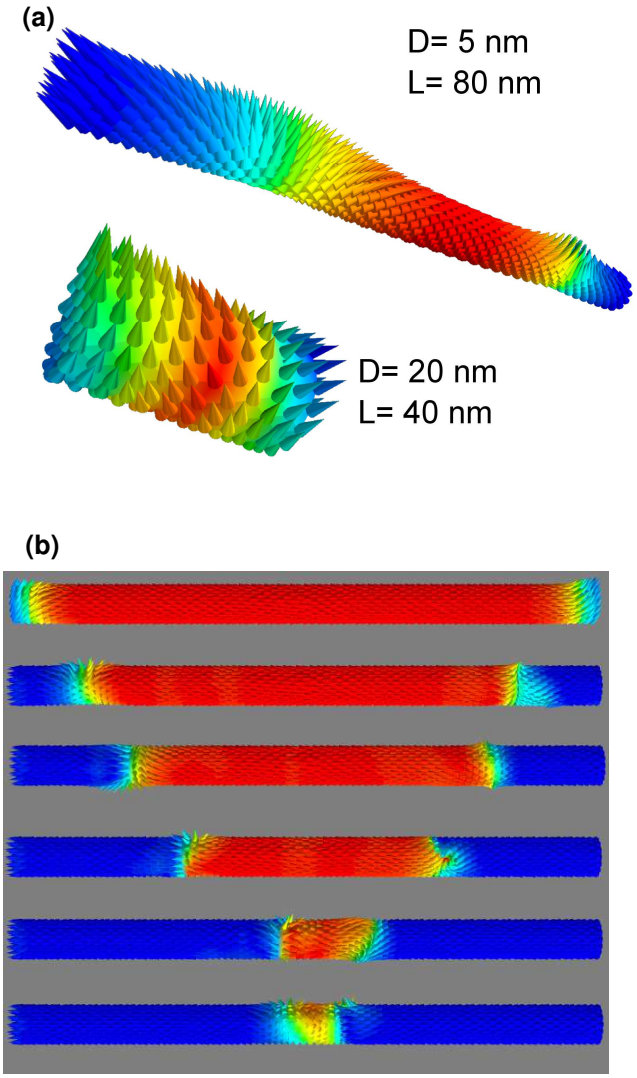

Figure 6 (a) Magnetic states close to the coercivity of Co cylinders with different diameters and aspect ratios. The colour variation corresponds to the magnetization component along the cylinder axis. The external field is applied with an angle $\psi = 5°$ relative to the cylinder axis. (b) Magnetic reversal in a Co cylinder with D = 20 nm and L = 16D. The colour variation corresponds to the magnetization component along the cylinder axis. The reversal proceeds with simultaneous propagation of two domain walls (tail-to-tail and head-to-head) towards the center following nucleation of reversed domains from the left and the right side respectively. The external field is applied with an angle $\psi = 5°$ relative to the cylinder axis.

results indicate that in both cases the reversal starts by nucleation at both wire edges and propagation of two domain walls towards the center (Figure 6).
Of course, in bundles of wires, in the majority of the cases, nucleation begins at one of the two edges, whichever is favored by the local interactions present. In shorter cylinders (figure 6a), no clear distinction between nucleation and non-uniform collective rotation can be made as the size of the nuclei are comparable to the whole sample size. This nucleation based reversal process explains why the structural coherence rather than the real length determines the coercivity (Figure 3c), as the stacking faults may also serve as nucleation centers just as the wire tips do. It should be noted that for small diameters the nucleation field has an angular and aspect ratio dependence similar to that of the SW model. It thus leads to a macroscopic behavior that it is not easily distinguished from that of SW particles.

4. Conclusion

Co nanorods with hcp structure have been produced by a chemical process which allows the control of the diameter and aspect ratio. The structural study showed that the increase of aspect ratio does not increase automatically the coherence length along the c axis because of stacking faults. The magnetic properties are strongly dependent on the rods morphology and structure. We showed that a short crystallographic aspect ratio is detrimental for the coercivity. The highest coercivities (up to 0.72 T) have been obtained for the sample exhibiting both the smallest mean diameter and the largest structural coherence aspect ratio. The longest rods generally exhibited a lower coercivity as a consequence of a higher amount of stacking faults along the rod axis. Micromagnetic simulations show that the reversal is dominated by nucleation at the rod edges, even for the smaller diameter wires. Coercivity increases with the aspect ratio but this effect fades away when the diameter increases. For diameter larger than 15 nm, there is no further increase of H_C for aspect ratio above 5. The increase of coercivity with decreasing mean diameter was well reproduced by the simulations. Thus, in order to produce a high strength magnet based on Co nanowires moderate aspect ratios of 5-10 are sufficient. This study shows that the priority is to avoid stacking faults in order to get a structural aspect ratio similar to the morphological aspect ratio. Very high coercivity

values were recently obtained with chemically grown cobalt nanorods of diameter 15 nm (ref. 5). It would be interesting to know if this new process allows a gain of crystallinity to confirm our conclusions.

Acknowledgements

This work was supported from the European Commission FP7 for the REFREEPERMAG (EU NMP3-SL-2012-280670) project.

References

[1] Krahne, R.; Morello, G.; Figuerola, A.; George, C.; Deka, S.; Manna, L. Physical Properties of Elongated Inorganic Nanoparticles. *Phys. Rep.* **2011**, *501*, 75–221.

[2] Liakakos, N.; Blon, T.; Achkar, C.; Vilar, V.; Cormary, B.; Tan, R. P.; Benamara, O.; Chaboussant, G.; Ott, F.; Warot-Fonrose, B.; et al. Solution Epitaxial Growth of Cobalt Nanowires on Crystalline Substrates for Data Storage Densities beyond 1 Tbit/in^2. *Nano Lett.* **2014**, *14*, 3481–3486.

[3] Schrittwieser, S.; Ludwig, F.; Dieckhoff, J.; Soulantica, K.; Viau, G.; Lacroix, L.-M.; Lentijo, S. M.; Boubekri, R.; Maynadié, J.; Huetten, A.; et al. Modeling and Development of a Biosensor Based on Optical Relaxation Measurements of Hybrid Nanoparticles. *ACS Nano* **2012**, *6*, 791–801.

[4] Maurer, T.; Ott, F.; Chaboussant, G.; Soumare, Y.; Piquemal, J.-Y.; Viau, G. Magnetic Nanowires as Permanent Magnet Materials. *Appl. Phys. Lett.* **2007**, *91*, 172501.

[5] Gandha, K.; Elkins, K.; Poudyal, N.; Liu, X.; Liu, J. P. High Energy Product Developed from Cobalt Nanowires. *Sci. Rep.* **2014**, *4*, 5345.

[6] Harris, V. G.; Chen, Y.; Yang, A.; Yoon, S.; Chen, Z.; Geiler, A. L.; Gao, J.; Chinnasamy, C. N.; Lewis, L. H.; Vittoria, C.; et al. High Coercivity Cobalt Carbide Nanoparticles Processed via Polyol Reaction: A New Permanent Magnet Material. *J. Phys.D: Appl. Phys.* **2010**, *43*, 165003.

[7] Poudyal, N.; Ping Liu, J. Advances in Nanostructured Permanent Magnets Research. *J. Phys. D: Appl. Phys.* **2013**, *46*, 043001.

[8] Balasubramanian, B.; Mukherjee, P.; Skomski, R.; Manchanda, P.; Das, B.; Sellmyer, D. J. Magnetic Nanostructuring and Overcoming Brown's Paradox to Realize Extraordinary High-temperature Energy Products *Sci. Rep.* **2014**, *4*, 6265.

[9] Soumare, Y.; Garcia, C.; Maurer, T.; Chaboussant, G.; Ott, F.; Fiévet, F.; Piquemal, J.-Y.; Viau, G. Kinetically Controlled Synthesis of Hexagonally Close-Packed Cobalt Nanorods with High Magnetic Coercivity. *Adv. Funct. Mater.* **2009**, *19*, 1971–1977.

[10] Soulantica, K.; Wetz, F.; Maynadié, J.; Falqui, A.; Tan, R. P.; Blon, T.; Chaudret, B.; Respaud, M. Magnetism of Single-Crystalline Co Nanorods. *Appl. Phys. Lett.* **2009**, *95*, 152504.

[11] Fang, W.; Panagiotopoulos, I.; Ott, F.; Boué, F.; Ait-Atmane, K.; Piquemal, J.-Y.; Viau, G.; Dalmas, F. Optimization of the Magnetic Properties of Aligned Co Nanowires/polymer Composites for the Fabrication of Permanent Magnets. *J. Nanoparticle Res.* **2014**, *16*, 2265.

[12] Skomski, R.; Zeng, H.; Zheng, M.; Sellmyer, D. J. Magnetic Localization in Transition-Metal Nanowires. *Phys. Rev. B* **2000**, *62*, 3900.

[13] Paulus, P. M.; Luis, F.; Kröll, M.; Schmid, G.; De Jongh, L. J. Low-Temperature Study of the Magnetization Reversal and Magnetic Anisotropy of Fe, Ni, and Co Nanowires. *J. Magn. Magn. Mater.* **2001**, *224*, 180–196.

[14] Bran, C.; Ivanov, Y. P.; Trabada, D. G.; Tomkowicz, J.; del Real, R. P.; Chubykalo-Fesenko, O.; Vazquez, M. Structural Dependence of Magnetic Properties in Co-Based Nanowires: Experiments and Micromagnetic Simulations. *IEEE Trans. Magn.* **2013**, *49*, 4491–4497.

[15] Schio, P.; Vidal, F.; Zheng, Y.; Milano, J.; Fonda, E.; Demaille, D.; Vodungbo, B.; Varalda, J.; de Oliveira, A. J. A.; Etgens, V. H. Magnetic Response of Cobalt Nanowires with Diameter below 5 nm. *Phys. Rev. B* **2010**, *82*, 094436.

[16] Ciuculescu, D.; Dumestre, F.; Comesaña-Hermo, M.; Chaudret, B.; Spasova, M.; Farle, M.; Amiens, C. Single-Crystalline Co Nanowires: Synthesis, Thermal Stability, and Carbon Coating. *Chem. Mater.* **2009**, *21*, 3987–3995.

[17] Liakakos, N.; Cormary, B.; Li, X.; Lecante, P.; Respaud, M.; Maron, L.; Falqui, A.; Genovese, A.; Vendier, L.; Koïnis, S.; et al. The Big Impact of a Small Detail: Cobalt Nanocrystal Polymorphism as a Result of Precursor Addition Rate during Stock Solution Preparation. *J. Am. Chem. Soc.* **2012**, *134*, 17922–17931.

[18] Aït-Atmane, K.; Michel, C.; Piquemal, J.-Y.; Sautet, P.; Beaunier, P.; Giraud, M.; Sicard, M.; Nowak, S.; Losno, R.; Viau, G. Control of the Anisotropic Shape of Cobalt Nanorods in the Liquid Phase: From Experiment to Theory… and Back. *Nanoscale* **2014**, *6*, 2682–2692.

[19] Viau, G.; Garcıa, C.; Maurer, T.; Chaboussant, G.; Ott, F.; Soumare, Y.; Piquemal, J.-Y. Highly Crystalline Cobalt Nanowires with High Coercivity Prepared by Soft Chemistry. *Phys. Status Solidi A* **2009**, *206*, 663–666.

[20] Aharoni, A. *Introduction to the Theory of Ferromagnetism*; International Series of Monographs on Physics 109, Oxford University Press, 2nd Ed., 2000.

[21] Ott, F.; Maurer, T.; Chaboussant, G.; Soumare, Y.; Piquemal, J.-Y.; Viau, G. Effects of the Shape of Elongated Magnetic Particles on the Coercive Field. *J. Appl. Phys.* **2009**, *105*, 013915.

[22] Panagiotopoulos, I.; Fang, W.; Aït-Atmane, K.; Piquemal, J.-Y.; Viau, G.; Dalmas, F.; Boué, F.; Ott, F. Low Dipolar Interactions in Dense Aggregates of Aligned Magnetic Nanowires. *J. Appl. Phys.* **2013**, *114*, 233909.

[23] Vidal, F.; Zheng, Y.; Schio, P.; Bonilla, F. J.; Barturen, M.; Milano, J.; Demaille, D.; Fonda, E.; de Oliveira, A. J. A.; Etgens, V. H. Mechanism of Localization of the

Magnetization Reversal in 3 nm Wide Co Nanowires. *Phys. Rev. Lett.* **2012**, *109*, 117205.

[24] Panagiotopoulos, I.; Fang, W.; Ott, F.; Boué, F.; Aït-Atmane, K.; Piquemal, J.-Y.; Viau, G. Packing Fraction Dependence of the Coercivity and the Energy Product in Nanowire Based Permanent Magnets. *J. Appl. Phys.* **2013**, *114*, 143902.

[25] Rueff, J.-M.; Masciocchi, N.; Rabu, P.; Sironi, A.; Skoulios, A. Synthesis, Structure and Magnetism of Homologous Series of Polycrystalline Cobalt Alkane Mono- and Dicarboxylate Soaps. *Chem. – Eur. J.* **2002**, *8*, 1813–1820.

[26] Chakroune, N.; Viau, G.; Ricolleau, C.; Fiévet-Vincent, F.; Fiévet, F. Cobalt-Based Anisotropic Particles Prepared by the Polyol Process. *J. Mater. Chem.* **2003**, *13*, 312–318.

[27] Gandha, K.; Poudyal, N.; Zhang, Q.; Liu, J. P. Effect of RuCl3 on Morphology and Magnetic Properties of CoNi Nanowires. *IEEE Trans. Magn.* **2013**, *49*, 3273–3276.

[28] Maurer, T.; Zighem, F.; Ott, F.; Chaboussant, G.; André, G.; Soumare, Y.; Piquemal, J.-Y.; Viau, G.; Gatel, C. Exchange Bias in Co/CoO Core-Shell Nanowires: Role of Antiferromagnetic Superparamagnetic Fluctuations. *Phys. Rev. B* **2009**, *80*, 064427.

[29] Zeng, H.; Skomski, R.; Menon, L.; Liu, Y.; Bandyopadhyay, S.; Sellmyer, D. J. Structure and Magnetic Properties of Ferromagnetic Nanowires in Self-Assembled Arrays *Phys. Rev. B* **2002**, *65*, 134426.

[30] Skomski, R.; Coey, J. M. D. *Permanent Magnetism*; Institute of Physics Pub.: Bristol, UK; Philadelphia, PA, 1999.

[31] Fischbacher, T.; Franchin, M.; Bordignon, G.; Fangohr, H. A Systematic Approach to Multiphysics Extensions of Finite-Element-Based Micromagnetic Simulations: Nmag. *IEEE Trans. Magn.* **2007**, *43*, 2896–2898.